A comparative analysis of parallel SSHI and SEH for bistable vibration energy harvesters

Quentin Demouron, Adrien Morel, David Gibus, Aya Benhemou, Adrien Badel

A comparative analysis of parallel SSHI and SEH for bistable vibration energy harvesters

Quentin Demouron[1], Adrien Morel[1], David Gibus[1], Aya Benhemou[1] and Adrien Badel[1]

[1] SYMME, Université Savoie Mont Blanc, Annecy, France

E-mail: quentin.demouron@univ-smb.fr

Received xxxxxx
Accepted for publication xxxxxx
Published xxxxxx

Abstract

The present work focuses on ambient vibration energy harvesting. Specifically, this article deals with bistable piezoelectric energy harvesters which exhibits a wider bandwidth than linear oscillators. These complex systems require an energy extraction circuit to rectify their voltage to supply power to autonomous sensors. This energy extraction circuit needs to be optimized in order to increase the harvested power and even the bandwidth of piezoelectric energy harvesters. Because of the complex dynamics of bistable piezoelectric energy harvesters, there is a lack of simple and physically-insightful models in the literature that would allow the understanding and optimization of the extraction circuit. To address this issue, the present work derives closed-form models of a bistable piezoelectric energy harvester coupled to a passive and an active synchronous energy extraction circuit: respectively the standard energy harvesting circuit (SEH) and the parallel synchronized switch harvesting on inductor circuit (P-SSHI). Experimental measurements conducted on a custom bistable piezoelectric energy harvester demonstrate the validity of the proposed models with a relative error lower than 15% on the harvested power and the bandwidth. The proposed models allow to easily understand the influence of the P-SSHI circuit on the dynamics of a bistable piezoelectric energy harvester. Moreover, a comparison of the performance of the SEH and the P-SSHI circuits, valid for any bistable generator, is proposed. The latter shows that under low electromechanical coupling and low acceleration amplitude the P-SSHI circuit leads to multiply the maximum harvested power up to 4.3 compared to the SEH circuit, and the bandwidth by a factor of 2.3.

Keywords: Piezoelectric energy harvester, Nonlinear systems, Vibrations, SSHI, Bistability, Analytical model.

1. Introduction

For the past decades, energy harvesting has been fervently investigated in order to increase batteries lifetime or even supplant them as part of wireless sensors or ultra-low power electronic devices. Various ambient energy sources can be available in the surrounding of the supplied system, under various forms: mechanical [1], radiative [2], thermic [3], electromagnetic [4], etc. In some applications, solar radiations or thermal gradients may be relatively low and vibrations may constitute the only relevant energy source.

Piezoelectric energy harvesters (PEH) have been widely investigated as a mean to convert the mechanical energy of surrounding vibrations into electrical energy. To extract the electrical energy from the PEH and rectify the piezoelectric voltage, an energy extraction circuit (EEC) is needed. Energy extraction circuits are a crucial component of any energy harvesting system, and require careful optimization to maximize the harvested power and bandwidth of the harvesting system. In the early stages of piezoelectric energy harvesting, passive EECs such as standard energy harvesting (SEH) were investigated, for instance, by Ottman et al. in 2002 [5]. However, the performance of such circuits were relatively limited in terms of the harvested power due to low electrically induced damping and low electromechanical coupling of the

harvesters. In order to increase the harvested power, active synchronous strategies like serial synchronized switch harvesting on inductor (S-SSHI) or parallel synchronized switch harvesting on inductor (P-SSHI) have been investigated by Guyomar et al. [6] in 2005. When coupled to a linear PEH, the P-SSHI circuit has been demonstrated to be particularly efficient in terms of power gain when the PEH exhibits a weak electromechanical coupling or an imposed displacement. However, for strongly coupled linear PEH, the P-SSHI circuit does not provide any power gain compared to the SEH circuit. Furthermore, even when combined with a P-SSHI circuit, the bandwidth of linear PEH is not increased. In 2005, Lefeuvre et al. proposed the synchronous electric charge extraction (SECE) [7]. Thereafter, from 2008 to 2019, various variants of the aforementioned strategies were optimized to further improve their performance, especially in terms of power density. These optimizations led to enhanced strategies like the double synchronized switch harvesting (DSSH) (Lallart et al. 2008 [8]), the multi-shot SECE (MSSECE) (Gasnier et al. 2014 [9]) and recently the synchronized switch harvesting on oscillator (SSHO) (Lallart et al. 2019 [10]). All these EECs have been investigated in combination with linear PEH. However, while these EECs increase the harvested power and the electrical efficiency, and reduce the dependency on load variations, the bandwidth of linear PEH remains relatively narrow.

In order to increase the bandwidth of vibration energy harvesters, nonlinear bistable mechanical resonators have been proposed by Stanton et al. in 2010 [11]. Due to their high-energy orbits, bistable PEH have been shown to significantly broaden the harvesting bandwidth [12]. Moreover, the mechanical displacement of the inertial mass on inter-well motion (high-energy orbit) is imposed, as demonstrated by Morel et al. in 2022 [13] which makes the P-SSHI especially suitable to increase the performance of bistable PEH. However, to date and to the authors knowledge, most of the papers focused on the study of mutual influence of nonlinear PEH and load resistance [14] - [16]. Only a few papers focus on the joint study and modelling of nonlinear EEC with nonlinear PEH. A numerical and experimental study of a bistable PEH paired with a SSHI circuit has been proposed by Singh et al. [17] in 2015. In this work, the authors demonstrated the interest of such a combination in order to increase the harvested power of the system under broadband excitations. Moreover, the harvested power has been compared to the one reached with SECE and SEH circuits. However, this study does not propose any analytical expressions allowing to understand the mutual influence of the nonlinear EEC and the bistable PEH. Thereafter, in 2019, an analytical and experimental study of a SECE circuit paired with a bistable PEH has been proposed by Huguet et al. [18]. In this work, the authors developed the first analytical model able to predict the frequency response of a bistable PEH coupled to a nonlinear EEC. A new relationship has been established between the piezoelectric voltage and the mechanical displacement in order to solve the system of equations. However, while analytical, the expressions obtained from the harmonic balance method and modelling the frequency response of the bistable PEH are particularly complex and cumbersome compared to closed-form models which allow to understand the mutual influence of EECs and bistable PEH in a physically-insightful way. Moreover, this study has been conducted on the SECE circuit which is, from the authors' point of view which is detailed after, not the most suitable circuit for bistable PEH. In addition, this study does not propose any comparison of the performance of different EECs. In 2020, an analytical modeling of nonlinear monostable PEH combined with nonlinear EEC has been proposed by Wang et al. [19]. In this study, the authors focused on deriving analytical solutions of different nonlinear EECs based on the impedance model. However, while simpler than the ones obtained by Huguet et al. the expressions remain complex and hinder the physically-insightful understanding of the mutual influence of the EECs and bistable PEH. Moreover, this study has been conducted on a nonlinear monostable PEH and is not valid for bistable PEH which are the most used for energy harvesting applications.

Since the P-SSHI circuit is known to be especially efficient when PEH exhibit an imposed displacement, the P-SSHI circuit seems to be especially suitable for bistable piezoelectric energy harvesters in order to increase the harvested power and the bandwidth. The aim of this paper is therefore to study the dynamics of bistable PEH connected to the P-SSHI circuit and to quantify the performance gain compared to the SEH circuit. In order to understand the mutual influence of the bistable PEH paired with the P-SSHI and the SEH circuit, the present study derives closed-form models of the two EECs in a physically-insightful way. Closed-form expressions of the electrical damping, extracted power, displacement amplitude and critical angular frequency (the frequency at which the inter-well motion disappears) are obtained. Moreover, these models allow to identify the conditions (frequency, electromechanical coupling, acceleration amplitude) that make the P-SSHI circuit more efficient than the SEH for bistable piezoelectric energy harvesting.

The second section of the paper presents the electromechanical model of the bistable PEH obtained for the inter-well motion. The closed-form expressions of the critical angular frequency and the displacement amplitude are derived based on a truncated harmonic balance. Based on Fourier series, the analytical expressions of the electrically induced damping and the damping ratio are obtained for the P-SSHI

and the SEH circuits. Thereafter, the expression of the harvested power is derived based on the harmonic balance. After the description of the experimental setup and protocol, an experimental validation of the closed-form model is proposed in the third section. This validation has been conducted on a custom-made bistable PEH and custom-made P-SSHI and SEH circuits. A performance comparison of the P-SSHI and SEH circuits, valid for any bistable PEH is finally presented in the fourth section of the present paper.

2. Electromechanical model of bistable PEH

This section presents the electromechanical model of bistable PEH and the assumptions considered in the rest of this paper. Subsequently, using truncated harmonic balance, closed-form expressions of the displacement amplitude, critical angular frequency and harvested power are derived.

2.1 Bistable PEH dynamics

A bistable PEH includes a nonlinear bistable mechanical resonator. Ambient vibrations are used as mechanical energy source to put an inertial mass in movement. The kinetic energy of the inertial mass is converted in electrical energy by mean of an electromechanical transducer. Many types of transducers (e.g. electromagnetic or piezoelectric) have been investigated for the past decades. This paper focuses on a piezoelectric energy harvester, specifically a bistable PEH.
The bistable PEH presented in **Figure 1** is made of an inertial mass and parallel buckled beams connected to an amplified piezoelectric actuator (APA) whose direct piezoelectric effect is used. The APA consists in an elliptical metallic shell in which a stack of lead titano-zirconate ceramic is installed. Depending on the position of the mass, the metallic shell is compressed or stretched, which results respectively in generating a negative or a positive voltage across the piezoelectric element.

The electromechanical dynamics of the bistable PEH has been modelled in previous work [20] by a set of differential equations:

$$\begin{cases} \gamma(t) = \ddot{x} + \dfrac{\omega_0}{Q}\dot{x} + \dfrac{\omega_0^2}{2}\left(\dfrac{x^2}{x_0^2} - 1\right)x + \dfrac{2\alpha}{ML}xv_p \\ C_p\dot{v_p} = \dfrac{2\alpha x\dot{x}}{L_{beam}} - i_p \end{cases} \quad (1)$$

In (1), x_0 and x stand for the equilibrium position and the displacement of the mass. α corresponds to the piezoelectric force factor. v_p and i_p are respectively the piezoelectric voltage and current. L_{beam}, M, C_p, Q and ω_0 are intrinsic parameters of the prototype and stand respectively for the buckled beams length, the inertial mass, the piezoelectric clamped capacitance, the mechanical quality factor and the natural frequency of the PEH.

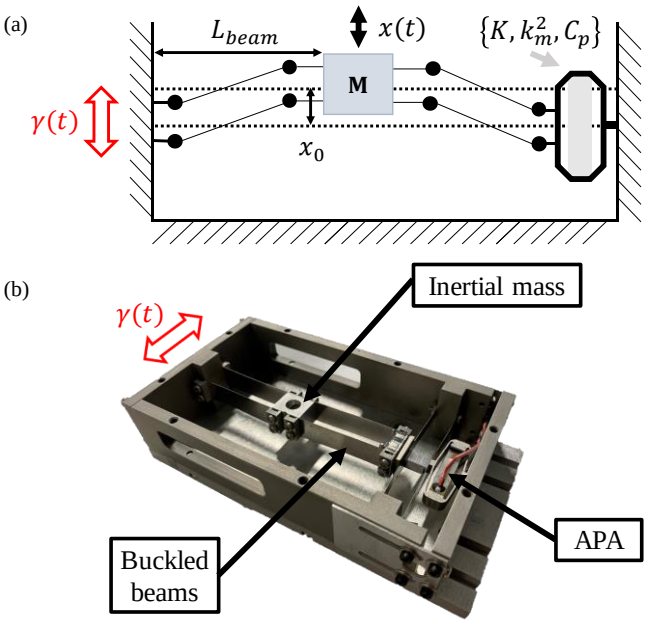

Figure 1 Schematic (a) and prototype (b) of bistable piezoelectric energy harvester.

Note that ω_0 and Q are obtained for the equivalent linear PEH, considering small displacement of the mass around one of the two equilibrium positions [20]. Note that in (1), the dielectric losses in the piezoelectric transducer are not considered since they are assumed to be negligible. In this study, we focused on a sinusoidal vibration which corresponds to many real-life cases [21]. Assuming that the vibration is sinusoidal, the acceleration is expressed as $\gamma(t) = \gamma_m \cos(\omega t + \psi)$ where γ_m is the acceleration amplitude, ω is the angular frequency and ψ is the phase. Assuming that the harmonics of the mass displacement remains low [22], it is expressed as $x(t) = x_m \cos(\omega t)$ with x_m its amplitude. Such assumption will be experimentally confirmed in section 3.2.

The bistable PEH may exhibits two types of orbits: intra-well and inter-well motions [23]. Intra-well motion is obtained for small displacement of the mass around one of the two equilibrium positions $x = \pm x_0$ whereas inter-well motion is obtained for large displacement of the mass around the two equilibrium positions. Since inter-well motion leads to a higher level of harvested power than intra-well motion, this paper focuses on the analysis of the first one. Note that inter-well motion can be reached applying orbit jump strategies. Reaching the inter-well motion with these strategies is not an easy task but promising works are conducted on this topic as detailed in [24] and [25].

As detailed in [14] and [26], the electrical term $\left(\frac{2\alpha}{ML_{beam}}xv_p\right)$ included in the mechanical equation of (1) represents the electrically induced damping corresponding to

the electrical energy extracted from the PEH. The first equation of (1) is reformulated to show the damping ratio β:

$$\gamma(t) = \ddot{x} + \frac{\omega_0}{Q}\dot{x}(1+\beta) + \frac{\omega_0^2}{2}\left(\frac{x_0^2}{2} - 1\right)x \qquad (2)$$

The damping ratio β corresponds to the ratio between the electrical damping D_e and the mechanical damping D_m. Note that the expression and value of β strongly depends on the EEC connected to the bistable PEH as presented in section 2.2 and 2.3.

The harmonic balance method already presented in [27] for a bistable PEH connected to a resistive load, is applied to (2). Note that only the first harmonic of the displacement is considered since its waveform is assumed to be close to a sine wave. Applying the harmonic balance method on (2) with $x(t) = x_m \cos(\omega t)$ leads to:

$$\begin{aligned}&\sin(\omega t)\left[\gamma_m \sin(\psi) - \frac{\omega_0}{Q}\omega x_m - \frac{\omega_0\beta}{Q}\omega x_m\right] \\ &+ \cos(\omega t)\left[-\gamma_m \cos(\psi) + \frac{3\omega_0^2}{2x_0^2}\frac{x_m^3}{4} - \frac{\omega_0^2}{2}x_m - \omega^2 x_m\right] = 0\end{aligned} \qquad (3)$$

Solving (3) is equivalent to solve the following equations:

$$\begin{cases} \gamma_m \sin(\psi) = \dfrac{\omega_0}{Q}\omega x_m + \dfrac{\omega_0\beta}{Q}\omega x_m \\ \gamma_m \cos(\psi) = \dfrac{3\omega_0^2}{2x_0^2}\dfrac{x_m^3}{4} - \dfrac{\omega_0^2}{2}x_m - \omega^2 x_m \end{cases} \qquad (4)$$

Summing and squaring the two equations of (4) leads to:

$$\begin{aligned}&\left(\frac{3x_m^2}{8x_0^2} - \frac{\omega_0^2}{2\omega^2} - 1\right)^2 + \left(\frac{\omega_0}{Q\omega}(1+\beta)\right)^2 \\ &- \left(\frac{\gamma_m}{x_m\omega^2}\right)^2 = 0\end{aligned} \qquad (5)$$

Considering that most of the bistable PEH have a high quality factor ($Q \simeq 100$) and that the effective acceleration of the inertial mass is much larger than the vibration acceleration in inter-well motion, the two last terms of (5) can be neglected in most cases, which leads to:

$$\left(\frac{3x_m^2\omega^2}{8x_0^2} - \frac{\omega_0^2}{2} - \omega^2\right)^2 = 0 \qquad (6)$$

Therefore, the expression of the displacement amplitude x_m is obtained solving (6):

$$x_m = \frac{2}{\sqrt{3}}x_0\sqrt{1 + \frac{2\omega^2}{\omega_0^2}} \qquad (7)$$

From (7), it is shown that the amplitude of the displacement x_m does not depend on the damping ratio β (provided that the inter-well orbit exists). Therefore, for a given frequency, the amplitude of the displacement is fully independent of the EEC. For bistable PEH, the resonance corresponds to the frequency for which the amplitude of the inter-well motion is maximal before the orbit suddenly disappears. This frequency is called *critical angular frequency* in the following. Under the assumption of the resonance ($\omega = \omega_c$), a phase lag of 90° exists between the acceleration amplitude and the maximum displacement [28]. Replacing $\psi = 90°$ in (4) leads to:

$$\begin{cases} \dfrac{\omega_0}{Q}\omega_c x_m + \dfrac{\omega_0\beta}{Q}\omega_c x_m = \gamma_m \\ \dfrac{3\omega_0^2}{2x_0^2}\dfrac{x_m^3}{4} - \dfrac{\omega_0^2}{2}x_m - \omega_c^2 x_m = 0 \end{cases} \qquad (8)$$

From (8), yields the expression of the critical angular frequency ω_c:

$$\omega_c = \sqrt{\frac{-\omega_0^2 + \sqrt{\omega_0^4 + \dfrac{6Q^2\gamma_m^2}{x_0^2(1+\beta)^2}}}{4}} \qquad (9)$$

From (9), it is shown that the critical angular frequency ω_c depends on the electrical damping. Therefore, the higher the electrical damping, the lower the critical angular frequency and conversely. Since the ratio of electrical and mechanical damping, β, depends on the EEC, its expression and impact on the dynamics of the PEH can be analytically modelled for each circuit.

2.2 Standard Energy Harvesting

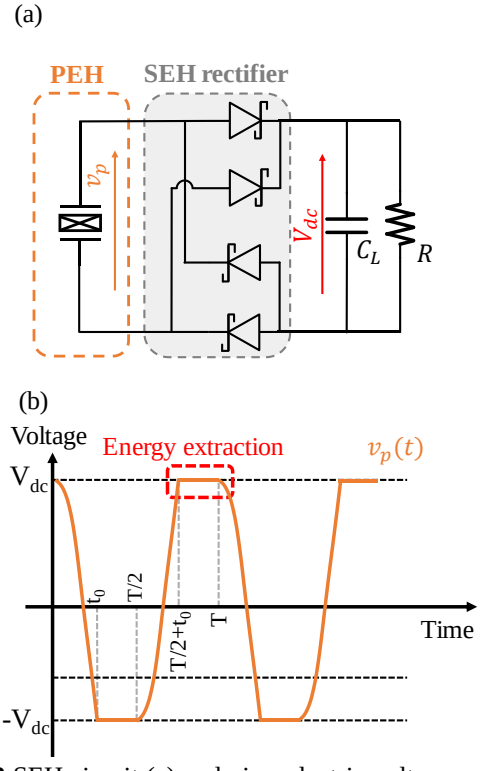

Figure 2 SEH circuit (a) and piezoelectric voltage waveform (b).

This section proposes an analysis of the dynamics and characteristics of the system when the bistable PEH is connected to the SEH circuit presented in **Figure 2.a**. As illustrated in **Figure 2.b**, during the time interval $[0, t_0]$, the piezoelectric voltage v_p decreases from V_{dc} to $-V_{dc}$. During the time interval $\left[t_0, \frac{T}{2}\right]$, the piezoelectric voltage is equal to the rectified voltage $-V_{dc}$. The rectifier bridge is conducting and the piezoelectric energy is transferred to the storage capacitor C_L. When $t = \frac{T}{2}$, the piezoelectric voltage begins to increase and the rectifier bridge is blocked. Afterwards, another half-period of vibration begins and the process is repeated. Note that the piezoelectric transducer is constrained twice per vibration period which results in the voltage frequency being twice the vibration frequency [20].

The piezoelectric voltage waveform on a half-period can be expressed as follows:

$$\begin{cases} v_p(t) = V_{dc} + \dfrac{1}{C_p}\displaystyle\int_0^t \alpha \dot{x}\, dt \;\forall t \in [0, t_0] \\ v_p(t) = -V_{dc} \;\forall t \in \left[t_0, \dfrac{T}{2}\right] \end{cases} \tag{10}$$

The piezoelectric voltage is periodic and can be expressed as a Fourier series for which only the first-order coefficients a_1 and b_1 are calculated:

$$\begin{cases} a_1 = \dfrac{4}{T}\displaystyle\int_0^{\frac{T}{2}} v_p(t)\cos(2\omega t)\, dt \\ b_1 = \dfrac{4}{T}\displaystyle\int_0^{\frac{T}{2}} v_p(t)\sin(2\omega t)\, dt \end{cases} \tag{11}$$

Therefore, the piezoelectric voltage expression of the fundamental is expressed as follows:

$$\begin{cases} v_p(t) = a_1\cos(2\omega t) + b_1\sin(2\omega t) \\ a_1 = \dfrac{\alpha x_m^2}{2C_p L_{beam}}\dfrac{2r\Omega}{2r\Omega + \frac{\pi}{2}} \\ b_1 = \dfrac{\alpha x_m^2}{2C_p L_{beam}}\dfrac{2r\Omega}{(4r\Omega + \pi)^2} \end{cases} \tag{12}$$

The mechanical resonator formed by the bistable PEH exhibits a filtering behavior. Therefore, the impact of higher order harmonics of the piezoelectric voltage can be neglected and the Fourier coefficients are only expressed for the fundamental. In the expressions of a_1 and b_1, r is the normalized electrical resistance expressed as $r = RC_p\omega_0$. Ω stands for the normalized frequency and is expressed as $\Omega = \frac{\omega}{\omega_0}$.

Injecting (12) in the first equation of (1) leads to the expression of the electrical term:

$$\frac{2\alpha x v_p}{L_{beam}} = \frac{2\alpha}{L_{beam}}\left(\begin{array}{c} \dfrac{a_1 x_m}{2}(\cos(\omega t) - \cos(3\omega t)) \\ + \dfrac{b_1 x_m}{2}(\sin(\omega t) - \sin(3\omega t)) \end{array}\right) \tag{13}$$

Where $\frac{2\alpha}{L_{beam}}\left(\frac{a_1 x_m}{2}\cos(\omega t)\right)$ is the voltage term in phase with the mechanical velocity, which leads to the expression of the electrically induced damping D_{eSEH}:

$$D_{eSEH} = \frac{16\alpha^2 r\Omega}{C_p\omega(4r\Omega + \pi)^2} \tag{14}$$

Equation (14) leads to the equation of the damping ratio $\beta_{SEH} = \frac{D_{eSEH}}{D_m}$:

$$\beta_{SEH} = \frac{x_m^2}{x_0^2}\frac{k_m^2 Q}{\Omega}\frac{2r\Omega}{(4r\Omega + \pi)^2} \tag{15}$$

In (15), k_m^2 is the squared electromechanical coupling coefficient. From (15), it is proven that there exists a value of the resistance $\left(r = \frac{\pi}{4\Omega}\right)$ which maximizes the electrical damping and thus minimizes the critical frequency ω_c.

The extracted power P_{ext} is defined as the power dissipated in the electrical damper $\mu_{e_{SEH}}$:

$$P_{ext} = \frac{1}{T}\int_0^T \mu_{e_{SEH}}\dot{x}^2 dt = \frac{M\beta_{SEH}\omega_0\omega^2 x_m^2}{2Q} \tag{16}$$

Combining (16) and (15) leads to the expression of the extracted power:

$$\begin{cases} P_{ext} = \dfrac{2M\omega_0\omega^2 x_m^2 k_m^2}{3\Omega}\left(1 + \dfrac{2\omega^2}{\omega_0^2}\right)\varepsilon_{D_{SEH}} \\ \varepsilon_{D_{SEH}} = \dfrac{2r\Omega}{(4r\Omega + \pi)^2} \end{cases} \tag{17}$$

Where $\varepsilon_{D_{SEH}}$ is the normalized electrical damping of the circuit. Note that the diodes losses of the bridge rectifier are considered negligible. Therefore, the harvested power P_h is considered approximately equal to the extracted power P_{ext}:

$$P_h \simeq P_{ext} \tag{18}$$

Since both the displacement amplitude x_m and the angular frequency ω are maximized when the resonance occurs ($\omega = \omega_c$), the harvested power $P_{h_{|\omega=\omega_c}}$ is the maximum harvested power for a given damping ratio as demonstrated in [13]. Moreover, the harvested power $P_{h_{|\omega=\omega_c}}$ is maximized when $\beta = 1$ ($D_e = D_m$) and reaches the power limit of the PEH as broadly described in the literature [29][30]. The power transfer and losses in the overall system for the SEH circuit are summarized in **Figure 3**.

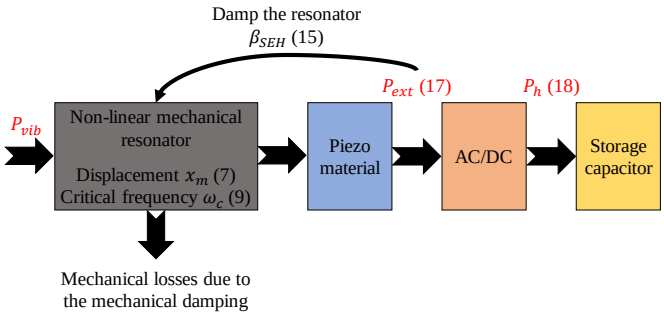

Figure 3 Power flow of the SEH circuit.

2.3 Parallel Synchronized Switch Harvesting on Inductor

This section proposes an analysis of the dynamics and characteristics of the system when the bistable PEH is connected to the P-SSHI circuit presented in **Figure 4.a**.

As illustrated in **Figure 4.b**, during the time interval $[0, t_0]$, the piezoelectric voltage v_p decreases until it reaches the rectified voltage $-V_{dc}$. When $t = t_0$, the piezoelectric voltage is equal to $-V_{dc}$, the rectifier bridge is conducting and the electrical energy is extracted from the piezoelectric transducer. During the time interval $\left[0, \frac{T}{2}\right]$, the electronic switch made of the two transistors is open. When $t = \frac{T}{2}$, the switch is closed.

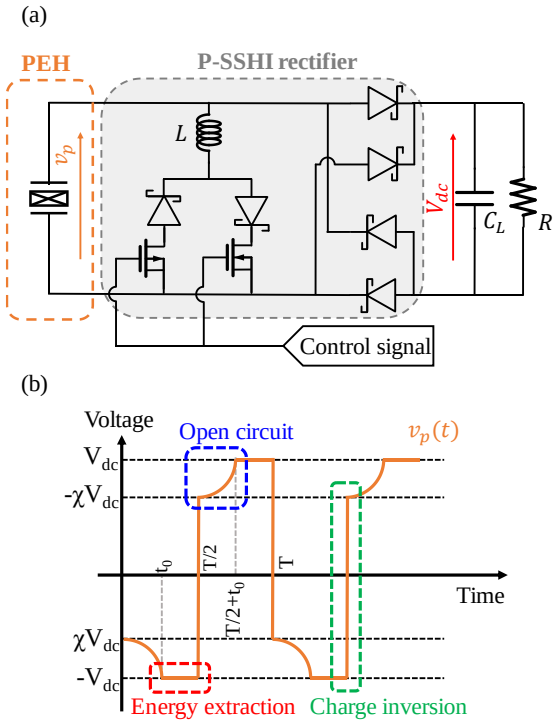

Figure 4 P-SSHI circuit (a) and piezoelectric voltage waveform (b).

The inductor L is connected to the piezoelectric capacitance C_p and due to this L-C loop, the piezoelectric voltage is quickly inverted. Afterwards, another half-period of vibration begins and the voltage processing is repeated. Note that the piezoelectric transducer is constrained twice per vibration period which results in the voltage frequency being twice the vibration frequency [20].

The piezoelectric voltage waveform on a half-period of vibration can be expressed as:

$$\begin{cases} v_p(t) = \chi V_{dc} + \int_0^t \frac{2\alpha x \dot{x}}{C_p L} dt \ \forall t \in [0, t_0] \\ v_p(t) = -V_{dc} \ \forall t \in \left[t_0, \frac{T}{2}\right] \end{cases} \quad (19)$$

$\chi = \frac{v_p\left(\frac{T}{2}^+\right)}{v_p\left(\frac{T}{2}^-\right)}$ is the voltage inversion ratio induced by the inductor L as illustrated in **Figure 4.a**. The piezoelectric voltage expression of the fundamental is expressed as follows:

$$\begin{cases} v_p(t) = a_1 \cos(2\omega t) + b_1 \sin(2\omega t) \\ a_1 = \frac{\alpha x_m^2}{2 C_p L_{beam}} \frac{1}{\left(1 + \frac{\pi}{2r\Omega(1-\chi)}\right)} \\ b_1 = \frac{\alpha x_m^2}{2 C_p L_{beam}} \frac{2r\Omega\left(\frac{2r\Omega(1-\chi^2)}{2\pi} + 1\right)}{\left((1+\chi)2r\Omega + \pi\right)^2} \end{cases} \quad (20)$$

Applying the same method as in section 2.2 leads to the expression of the electrically induced damping D_{ePSSHI}:

$$D_{ePSSHI} = \frac{16\alpha^2 r\Omega\left(\frac{2r\Omega(1-\chi^2)}{2\pi} + 1\right)}{C_p \omega \left((1+\chi)2r\Omega + \pi\right)^2} \quad (21)$$

From (21) yields the expression of the damping ratio $\beta_{PSSHI} = \frac{D_{ePSSHI}}{D_m}$:

$$\beta_{PSSHI} = \frac{x_m^2}{x_0^2} \frac{k_m^2 Q}{\Omega} \frac{2r\Omega\left(\frac{2r\Omega(1-\chi^2)}{2\pi} + 1\right)}{\left((1+\chi)2r\Omega + \pi\right)^2} \quad (22)$$

From (22), it is proven that a larger resistance leads to a larger damping ratio β. The extracted power P_{ext} corresponds to the power dissipated in the electrical damper D_{ePSSHI}:

$$P_{ext} = \frac{1}{T} \int_0^T D_{ePSSHI} \dot{x}^2 dt = \frac{M \beta_{PSSHI} \omega_0 \omega^2 x_m^2}{2Q} \quad (23)$$

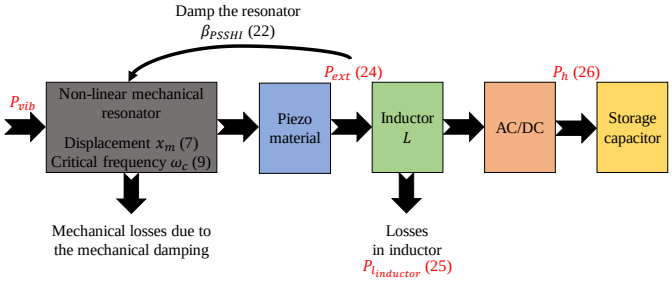

Figure 5 Power flow of the P-SSHI circuit.

Combining (23) and (22) leads to the expression of the extracted power:

$$\begin{cases} P_{ext} = \dfrac{2M\omega_0\omega^2 x_m^2 k_m^2}{3\Omega}\left(1+\dfrac{2\omega^2}{\omega_0^2}\right)\varepsilon_{D_{PSSHI}} \\ \varepsilon_{D_{PSSHI}} = \dfrac{2r\Omega\left(\dfrac{2r\Omega(1-\chi^2)}{2\pi}+1\right)}{\left((1+\chi)2r\Omega+\pi\right)^2} \end{cases} \quad (24)$$

As predicted from (24), the extracted power increases with the vibration frequency. Moreover, large resistance values lead to large damping ratio as proven from (22). Therefore, the critical angular frequency ω_c decreases as the resistance increases as proven from (9). As a consequence of the lower critical frequency that may be reached with the P-SSHI circuit, the harvested power at low vibration frequency is larger than with the SEH circuit as long as the inter-well motion exists., The losses $P_{l_{inductor}}$ in the inductor L during the piezoelectric voltage inversion [29] can be expressed as:

$$P_{l_{inductor}} = \frac{2r\Omega(1-\chi^2)}{2\pi+2r\Omega(1-\chi^2)}P_{ext} \quad (25)$$

Therefore, the harvested power P_h is lower than the extracted power P_{ext} and is expressed as:

$$P_h = \frac{2\pi}{2\pi+2r\Omega(1-\chi^2)}P_{ext} \quad (26)$$

Figure 5 summarizes the power transfer and losses in the overall system for the P-SSHI circuit.

3. Experimental validation

3.1 Experimental setup and protocol

In order to validate the proposed models, a custom-made prototype of bistable harvester has been developed. The prototype is presented in **Figure 1**. The parameters of the equivalent linear model $(Q, \omega_0, k_m^2, C_p$ and $M)$ have been experimentally identified on the intra-well motion under weak sinusoidal excitation and are summarized in **Table 1**. The length of the buckled beams L_{beam} has been measured on the prototype. The equilibrium position x_0 has been measured by mean of a laser vibrometer.

The P-SSHI circuit is presented in **Figure 4.a**. The circuit is made of two stages known as electronic switch and rectifier. As shown in **Figure 4.a**, the inductor, the Schottky diodes and the mosfet transistors constitute the electronic switch. The rectifier is made of 4 Schottky diodes and a filtering capacitor. The reference of the Nmos transistor is ZVN2110GTA whereas the reference of the Pmos transistor is IRFL9110TRPBF. The reference of the Schottky diodes are BAT43. Note that the SEH circuit is an adaptation of the P-SSHI circuit obtained from disconnecting the inductor L and the mosfet's driving signal.

Experimental measurements have been performed on the testbench shown in **Figure 6**. The bistable PEH is attached to an electromagnetic shaker. A dSpace realtime control system is used to receive and record signal from a differential vibrometer and an accelerometer and to drive the power amplifier (PA) which supplies the electromagnetic shaker. The vibration amplitude is maintained to a constant value thanks to a closed-loop control of the amplitude of the sinusoidal excitation. The piezoelectric transducer of the bistable PEH is connected to the EEC. A programmable resistor is connected to the output of the EEC. The piezoelectric voltage is recorded by the acquisition board through a voltage follower. The measurements of the displacement amplitude and speed of the mass are performed by the differential laser vibrometer. The waveforms of the displacement amplitude, speed, piezoelectric voltage and rectified voltage are stored for each combination of frequency, acceleration and resistance.

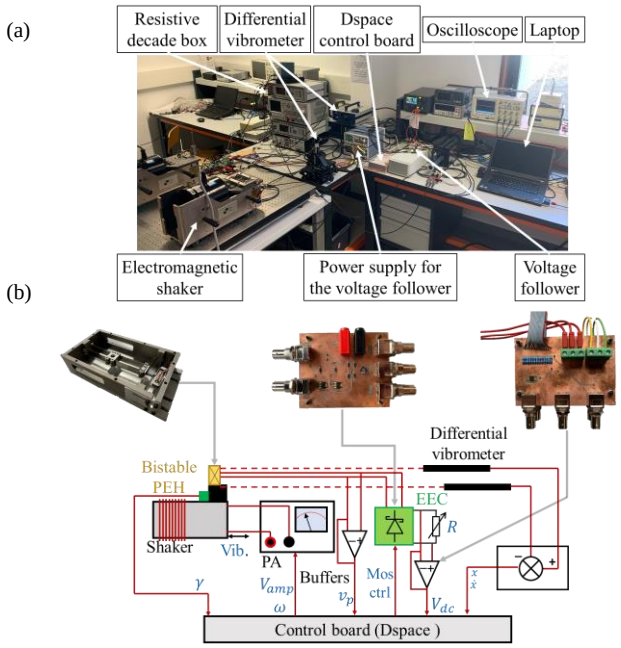

Figure 6 Experimental setup used for the validation of the models (a) and schematic of the setup (b).

Table 1 Experimentally identified parameters of the bistable PEH

Parameter	Variable	Value	Unit
Inertial mass	M	6.3	g
Length of a beam	L_{beam}	35	mm
Equilibrium position	x_0	0.74	mm
Natural frequency	ω_0	315	$rad.s^{-1}$
Mechanical quality factor	Q	90	–
Electromechanical coupling	k_m^2	0.063	–
Piezoelectric clamped capacitance	C_p	1.023	μF

The experimental characterization of the bistable PEH is performed in the inter-well motion. The complete characterization of the bistable PEH is obtained for 30 resistances between 100 Ω and 10 $k\Omega$ on a logarithmic scale and 90 frequencies from 25 Hz to 67 Hz on a linear scale. In the case of bistable PEH operating in inter-well motion, the displacement amplitude of the mass is roughly proportional to the vibration frequency [13]. Consequently, as the frequency increases, so do the displacement and the stresses within the beams and the APA. This stress can potentially result in plastic deformation or the failure of either the APA or the beams. In the present case, the upper bound of the frequency range had to be set at 67 Hz. In order to reach the inter-well motion, an orbit jump sequence has been developed. The experimental protocol for the bistable PEH characterization on the inter-well motion is detailed in appendix A.

3.2 Experimental validation of the proposed models

Figure 7 shows the experimental time signals of the phase space, the displacement amplitude, the piezoelectric voltage and the energy cycle for the SEH and P-SSHI circuit under an acceleration amplitude $\gamma_m = 11\, m.s^{-2}$ and a vibration frequency $f_{vib} = 35\, Hz$. As shown in **Figure 7.b** and **Figure 7.f**, the mechanical displacement remains close to a sinusoidal waveform, in the sense that the amplitude of higher order harmonics remains low compared to the amplitude of the fundamental, which justify the assumption of the first-order harmonic in section 2.1. **Figure 7.d** and **Figure 7.h** illustrate the energy cycle for both the SEH and the P-SSHI circuits. The area under the curve is associated to the energy extracted during a period of the displacement. Note that the deformation of the APA when $x = 0$ is different form the one when $x = \pm x_m$ which results in an asymmetry on the piezoelectric voltage. Note that this asymmetry is slightly more pronounced for the SEH circuit than the P-SSHI circuit and is not considered in the proposed model.

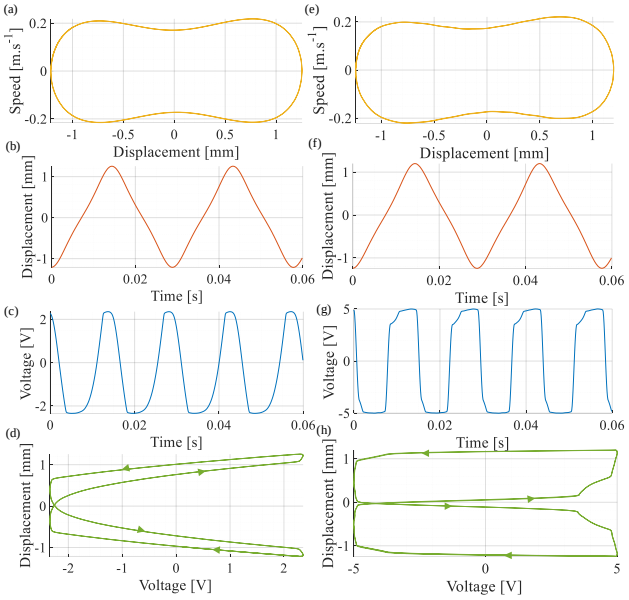

Figure 7 Phase space, displacement, voltage and energy cycle waveforms for the SEH (a. b. c. d.) and the P-SSHI (e. f. g. h.) with $\gamma = 5\, m.s^{-2}$.

The experimental measurements and the theoretical predictions of the harvested power as a function of the vibration frequency are shown for both the SEH and the P-SSHI in **Figure 8**. The experimental results are in good agreement with the theoretical predictions with less than 15% error on the harvested power and less than 5% error on the critical frequency. However, a slight mismatch can be observed for high vibration frequencies, due to the excitation of high-order internal modes of the electromagnetic shaker and mounting bracket. **Figure 8.a** (SEH circuit) shows that for $R = 4.5$ kΩ (red curves), the critical frequency $f_c = \frac{\omega_c}{2\pi}$ is above 67 Hz. As predicted from (15), the damping ratio increases with the resistance until it reaches a maximum for $r = \frac{\pi}{4\Omega}$ which corresponds to the optimal resistance minimizing the critical frequency. For resistance values larger than the optimal resistance, the damping ratio β_{SEH} decreases as the resistance increases, which results in the increase of the critical frequency. For $R = 1.3\, k\Omega$ (blue curves), the critical frequency is minimized and is around 63 Hz whereas it is above 67 Hz for $R = 7.3\, k\Omega$ (yellow curves). These results are in good agreement with the theoretical predictions from (9). The harvested power is also well predicted by the model.

Figure 8.b (P-SSHI circuit) shows that for $R = 574\, \Omega$ (blue curves), f_c is close to 60 Hz. As long as the resistance increases, the damping ratio β_{PSSHI} (22) increases which results in the decrease of the critical frequency as proven from (9). For $R = 4.5\, k\Omega$ (yellow curves), f_c is around 37 Hz. These results are in good agreement with the theoretical predictions from (9).

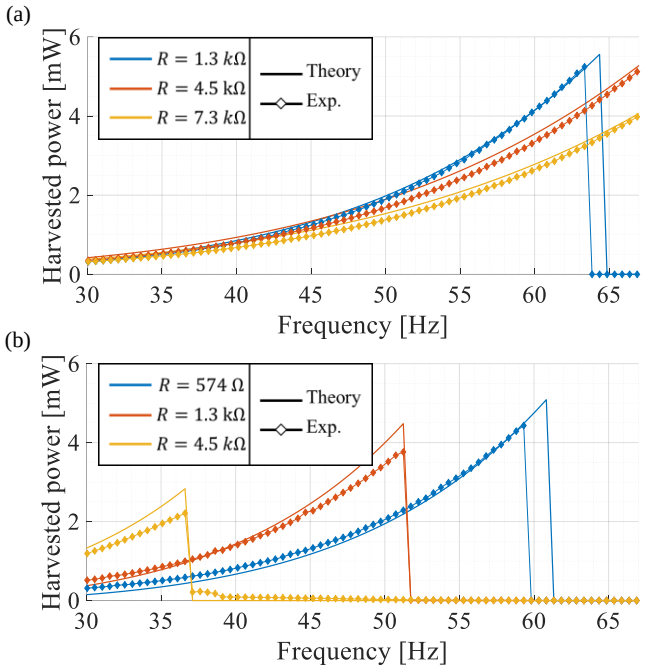

Figure 8 Experimental measurements (diamonds) and theoretical predictions (solid lines) of the harvested power for the SEH (a) and the P-SSHI (b), for three resistance values and $\gamma_m = 5\ m.s^{-2}$.

The harvested power is also in good agreement with the theoretical predictions, with less than 15% error.

The harvested power P_h as a function of the frequency and the load resistance for the SEH circuit for both the experimental measurements and the theoretical predictions is illustrated in **Figure 9**. The critical frequency f_c is shown to be a function of the resistance as proven from (9) and (15). For small or large resistance values ($R < 300\ \Omega$ or $R > 4\ k\Omega$), the critical frequency is close to 67 Hz. Between, these values, the critical frequency decreases up to 64 Hz. The minimal critical frequency occurs for $R = 1.27\ k\Omega$ which corresponds to the resistance $R = \frac{\pi}{4C_p\omega}$ where ω is the vibration angular frequency and C_p is the piezoelectric clamped capacitance. For this specific value of the resistance, the damping ratio β_{SEH} is greater than 1 and is maximized. This means that the electrical damping is greater than the mechanical damping and reaches its maximum value. The harvester is therefore overdamped and the critical frequency is minimized. As predicted by the model, the harvested power increases with the vibration frequency. For $R = 574\ \Omega$, the harvested power is about 3.2 mW with $f_{vib} = 60\ Hz$ whereas it is about 0.2 mW with $f_{vib} = 30\ Hz$. Comparing the experimental measurements (**Figure 9.a**) and the theoretical predictions (**Figure 9.b**), a slight mismatch is observed on the critical frequency (63.85 Hz for the experimental measurements vs 64.36 Hz for the theoretical model with $R = 1.27\ \Omega$). Note that this slight mismatch can be explained by the fairly strong assumptions of the proposed model.

Figure 10 shows the harvested power as a function of the frequency and the load resistance for the P-SSHI circuit for both the experimental measurements and the theoretical predictions. As for the SEH circuit, the critical frequency (9) is a function of the resistance. However, the higher the resistance, the higher the damping ratio β_{PSSHI} (22) and the lower the critical frequency. The critical frequency varies in an inversely proportional way from 30 Hz to 67 Hz as the resistance varies from 100 Ω to 10 $k\Omega$. As for the SEH circuit, the harvested power increases as the vibration frequency increases. However, compared to the SEH circuit, the harvested power is greater. As a matter of example, when $R = 1.3\ k\Omega$, the harvested power with the P-SSHI circuit is about 3.5 mW with $f_{vib} = 50\ Hz$ whereas it is about 0.5 mW with $f_{vib} = 30\ Hz$. Comparatively, when $R = 1.3\ k\Omega$ the harvested power with the SEH circuit is around 1.9 mW with $f_{vib} = 50\ Hz$ whereas it is around 0.3 mW with $f_{vib} = 30\ Hz$. Comparing the experimental measurements (**Figure 10.a**) and the theoretical predictions (**Figure 10.b**), it is shown that the slopes of the critical frequency are close to each other although a slight mismatch is observed under large displacement of the mass for high vibration frequencies.

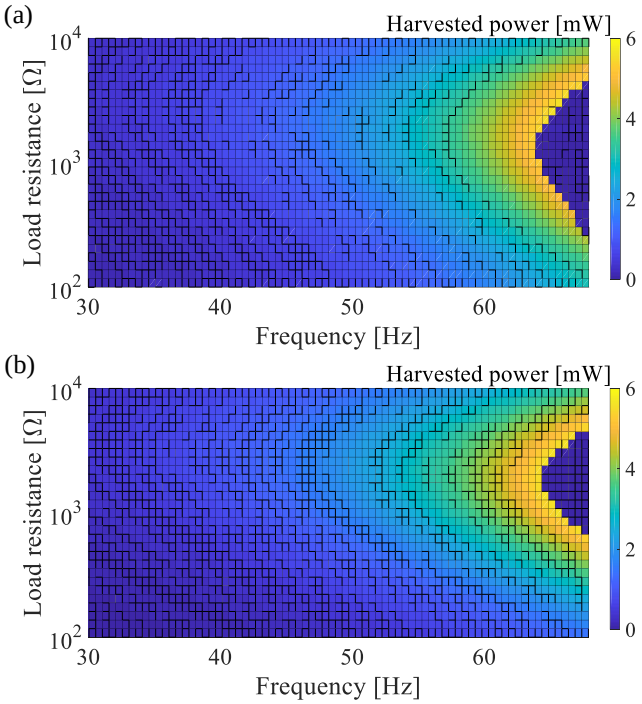

Figure 9 Experimental measurements (a) and theoretical predictions (b) of the harvested power as a function of the frequency and the load resistance for the SEH with $\gamma_m = 5\ m.s^{-2}$.

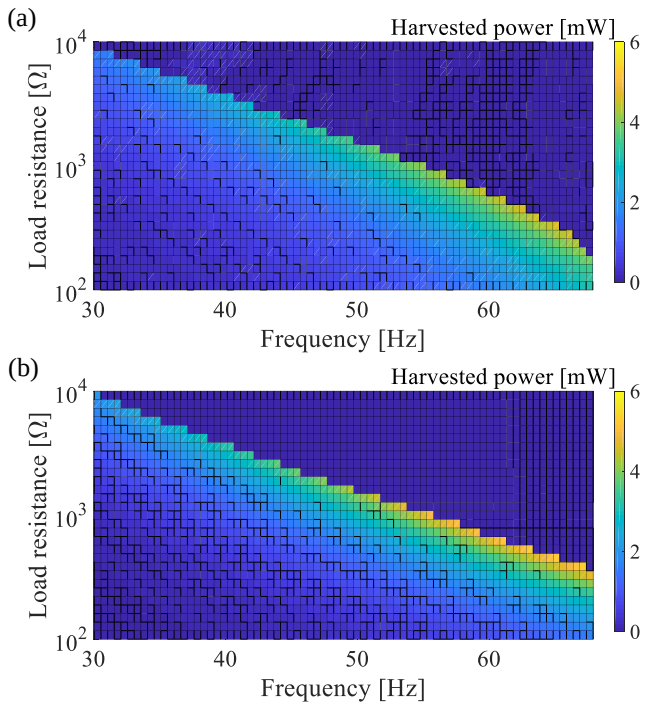

Figure 10 Experimental measurements (a) and theoretical predictions (b) of the harvested power as a function of the frequency and the load resistance for the P-SSHI with $\gamma_m = 5\ m.s^{-2}$.

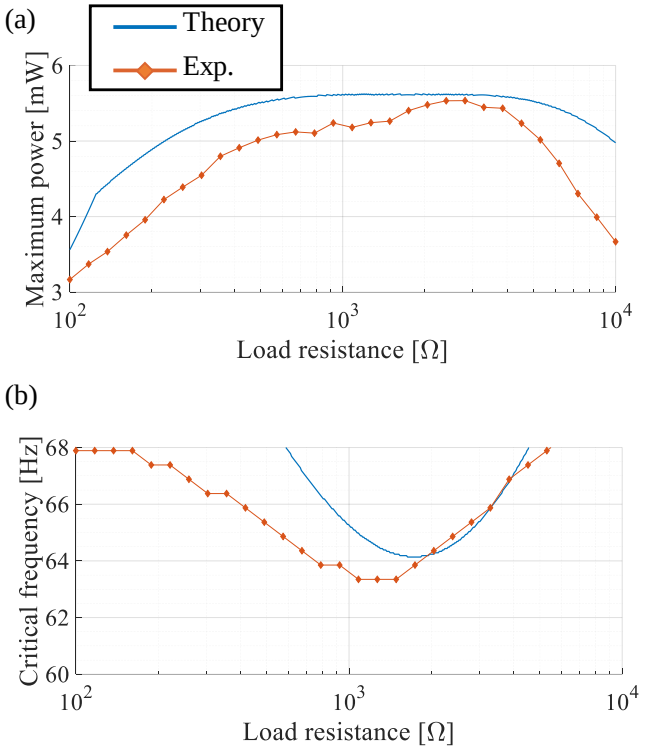

Figure 11 Experimental measurements (diamonds) and theoretical prediction (solid line) of the maximum harvested power (a) and critical frequency (b) as a function of the load resistance for the SEH with $\gamma_m = 5\ m.s^{-2}$.

Figure 11 illustrates the maximum harvested power $P_{h_{|\omega=\omega_c}}$ and the critical frequency f_c as a function of the load resistance for the SEH circuit and for both experimental measurements and theoretical predictions. The resistance maximizing the harvested power is not the one that maximizes the damping ratio. The harvested power experimentally reaches a maximum of $5.5\ mW$ for a load resistance of $2.4\ k\Omega$. For this specific value of the resistance, the damping ratio $\beta_{SEH} = 1$ which means that the electrical and the mechanical damping are both equal. On the other hand, the minimum critical frequency is reached for $R = 1.27\ k\Omega$. This resistance maximizes the damping ratio β thus overdamping the harvester and decreasing the harvested power. For small resistance values ($R < 500\ \Omega$) or large resistance values ($R > 3k\Omega$) the damping ratio β is low which results in a high critical frequency. For $\beta < 1$, the harvested power decreases with the damping ratio. Note that a slight mismatch can be observed on the harvested power between the theoretical predictions and the experimental measurements. The latter may be due to the asymmetry of the deformation of the APA which tends to decreases the effective electromechanical coupling thus decreasing the damping ratio β and the harvested power P_h.

Figure 12 illustrates the maximum harvested power $P_{h_{|\omega=\omega_c}}$ and the critical frequency f_c as a function of the load resistance for the P-SSHI circuit and for both the experimental measurements and the theoretical predictions. The harvested power experimentally reaches a maximum of $4.6\ mW$ for $R = 360\ \Omega$. On the other hand, the minimum critical frequency is reached for the largest value of the resistance ($R = 10\ k\Omega$ in this case). Increasing the resistance, leads to an increase of the damping ratio β as proven by (22). The P-SSHI circuit allows to reach much larger values of the damping ratio than the SEH circuit thus leading to harvest power on a larger bandwidth. As a matter of example, the maximum damping ratio β_{max} reaches 6.2 for the P-SSHI circuit whereas it is only 1.01 for the SEH circuit. Note that for both SEH and P-SSHI circuits, a trade-off must be found between the harvested power and the critical frequency. Indeed, high values of the damping ratio, lead to lower critical frequency. However, the harvested power is increased as long as the inter-well motion exists. Note that the mismatch observed on the harvested power can be explained by the efficiency of the P-SSHI circuit which is lower in experiment than in theory.

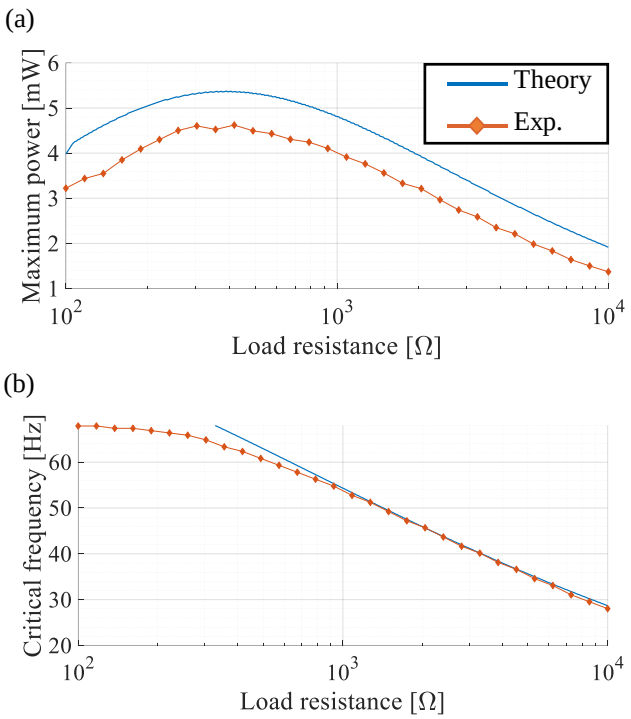

Figure 12 Experimental measurements (diamonds) and theoretical predictions (solid line) of the maximum harvested power (a) and the critical frequency (b) as a function of the load resistance for the P-SSHI with $\gamma_m = 5\ m.s^{-2}$.

This mismatch can be explained by the diodes and the switching losses that are not considered in the model.

4. Performance comparison

The present section offers a performance comparison of the P-SSHI and the SEH circuits. The influence of the electromechanical coupling and the acceleration amplitude has been studied in order to propose a generic comparison applicable to any bistable PEH.

The maximum harvested power as a function of the vibration frequency is illustrated in **Figure 13** for both the SEH and the P-SSHI with $\gamma_m = 5\ m.s^{-2}$. The maximum harvested power corresponds to the harvested power for each frequency and for which the resistance allowing to maximize the power is selected. It shows that for the SEH circuit and a vibration frequency of $35\ Hz$, the experimental maximum harvested power reaches $0.5\ mW$. At the same vibration frequency, the harvested power is multiplied by 4 for the P-SSHI circuit, thus reaching $2\ mW$. For the SEH circuit, the theoretical harvested power is in good agreement with the experimental measurements. Regarding the P-SSHI circuit, a mismatch can be observed between the experimental measurements and the theoretical predictions.

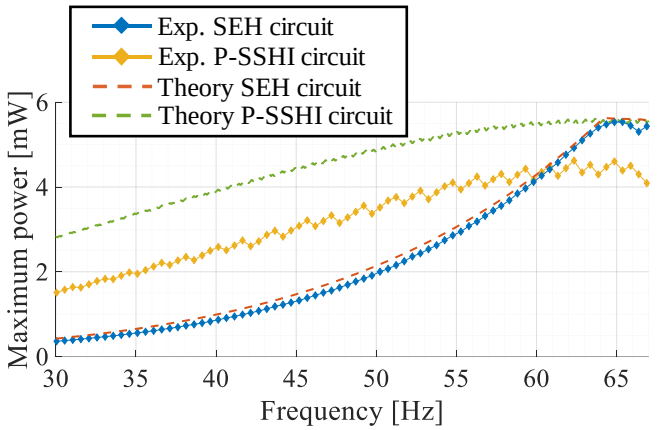

Figure 13 Experimental measurements (diamonds) and theoretical predictions (dashed line) of the maximum harvested power for the SEH (blue and orange) and the P-SSHI (yellow and green) with $\gamma_m = 5\ m.s^{-2}$.

There are two main reasons for this mismatch: the fairly strong assumptions of the model and the experimental efficiency of the P-SSHI circuit which is lower than in theory. Compared to the SEH circuit, the P-SSHI circuit allows to considerably increase the damping ratio β and thus to increase the harvested power under low vibration frequencies (between $30\ Hz$ and $60\ Hz$) as illustrated in **Figure 13**. Consequently, the bandwidth of the harvester, which is calculated as the frequency range for which the harvested power is greater than half of the maximum power, is increased ($28.88\ Hz$ for the P-SSHI circuit instead of $12.73\ Hz$ for the SEH circuit), as shown in **Figure 13**. Another interpretation of this bandwidth expansion is related to the ability of the P-SSHI circuit to vary the critical frequency over a larger range, as can be seen by comparing **Figure 11.b** and **Figure 12.b**. Note that in both cases (P-SSHI and SEH), the theoretical harvested power reaches a maximum of $5.5\ mW$ which correspond to the well-known power limit $P_{lim} = \frac{\gamma_m^2 QM}{8\omega_0}$ as described in [29] and [30]. However, due to a slightly lower efficiency, the harvested power of the P-SSHI circuit is smaller than that of the SEH circuit ($4.62\ mW$ for the P-SSHI circuit instead of $5.53\ mW$ for the SEH circuit) under high vibration frequencies (above $60\ Hz$). Note that the reduced efficiency can be attributed to the implementation of the circuit and the selection of components, which could be further optimized.

As presented previously, the power envelope corresponds to the harvested power for each frequency and for which the resistance allowing to maximize the power is selected. This power envelope varies according to the electromechanical coupling, the acceleration amplitude and the energy extraction circuit. **Figure 13** illustrates the power envelopes of the SEH and the P-SSHI circuits for an acceleration amplitude $\gamma_m = 5\ m.s^{-2}$ and an electromechanical coupling $k_m^2 = 6.3\ \%$.

From **Figure 13** the question of the evolution of the bandwidth with the electromechanical coupling can be asked. In order to compare the bandwidth of the harvester when connected to the P-SSHI or the SEH circuit, the bandwidth ratio of their respective power envelope is defined. This ratio can be expressed as:

$$BW_{Ratio} = \frac{\Delta_{w_{PSSHI}}}{\Delta_{w_{SEH}}} \quad (27)$$

In (27), Δ_w is the frequency range for which the harvested power is greater than half of the maximum power. **Figure 14** illustrates the bandwidth ratio as a function of the acceleration amplitude and the electromechanical coupling. For weak electromechanical coupling ($1-3$ %), the bandwidth ratio is below 1.63. For this range of electromechanical coupling, the bandwidth ratio is barely impacted by the acceleration amplitude: for $k_m^2 = 2$ % and $\gamma_m = 1\, m.s^{-2}$, the bandwidth ratio is around 1.52 whereas it is slightly above 1.64 for $k_m^2 = 2$ % and $\gamma_m = 10\, m.s^{-2}$. Increasing the electromechanical coupling tends to increase the bandwidth ratio. Under weak or strong electromechanical coupling, the P-SSHI circuit does not allow to considerably increase the bandwidth of the harvester in comparison to the SEH circuit. It is shown that the P-SSHI circuit exhibits an electromechanical coupling sweep spot for which the bandwidth is considerably increased. This sweet spot is called *critical coupling*.

For most of the acceleration amplitudes, the critical coupling is around 13 %. For this critical coupling, the bandwidth ratio is around 2.29. This means that the bandwidth of the harvester associated to the P-SSHI circuit is more than 2 times greater than the bandwidth of the harvester associated to the SEH circuit. For very strong electromechanical coupling (above 13%), the bandwidth ratio decreases until it reaches 1 which means that the P-SSHI circuit is then not more efficient than the SEH.

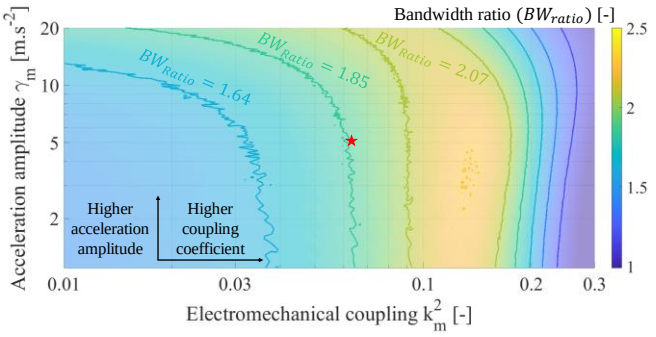

Figure 14 Bandwidth ratio (BW_{Ratio}) as defined in (27), as a function of the acceleration amplitude and the electromechanical coupling. The red star corresponds to the acceleration amplitude and coupling conditions of the experimental tests. Warmer colors correspond to higher values of the bandwidth ratio.

Note that the theoretical bandwidth ratio never drops below 1 which means that in the worst case, the P-SSHI circuit is equivalent to the SEH circuit in terms of bandwidth. However, due to the experimental efficiency of the P-SSHI circuit, which is lower than the theoretical one, the experimental bandwidth ratio can drop below 1 and the SEH circuit is thus better than the P-SSHI circuit, especially under frequencies above $60\, Hz$. Considering the bistable PEH presented in **Figure 1** which has an electromechanical coupling of about 6.3 %, the bandwidth ratio is close to 1.9 for the three experimental acceleration amplitudes (red stars) as shown in **Figure 14**.

The maximum harvested power ratio computed to quantify the power gain using the P-SSHI circuit is illustrated in **Figure 15**. This ratio can be expressed as:

$$P_{hmax_{Ratio}} = \frac{\max_{f\in\mathbb{R}^+}(\max_{R\in\mathbb{R}^+}(P_{h_{PSSHI}}))}{\max_{f\in\mathbb{R}^+}(\max_{R\in\mathbb{R}^+}(P_{h_{SEH}}))} \quad (28)$$

Where $\max_{f\in\mathbb{R}^+}(\max_{R\in\mathbb{R}^+}(P_h))$ is the maximum power for all frequencies of a power envelope which is itself the maximum power for each resistance. For weak electromechanical coupling ($1-3$ %) and weak acceleration amplitudes ($1-3\, m.s^{-2}$), the harvested power ratio is greater than 3.6 which means that the maximum harvestable power is multiplied by more than 3.6 using the P-SSHI circuit compared to the SEH. Increasing the acceleration amplitude for this range of electromechanical coupling tends to decrease the harvested power ratio. The latter decreases from 2.55 to 2.13 at $\gamma_m = 20\, m.s^{-2}$ whereas there is almost no decrease at $\gamma_m = 1\, m.s^{-2}$. Considering medium electromechanical coupling ($3-6$ %), the harvested power ratio decreases as the electromechanical coupling increases thus going from 3.7 at $k_m^2 = 3$ % and $\gamma_m = 1\, m.s^{-2}$ to 2.9 at $k_m^2 = 6$ % and $\gamma_m = 1\, m.s^{-2}$.

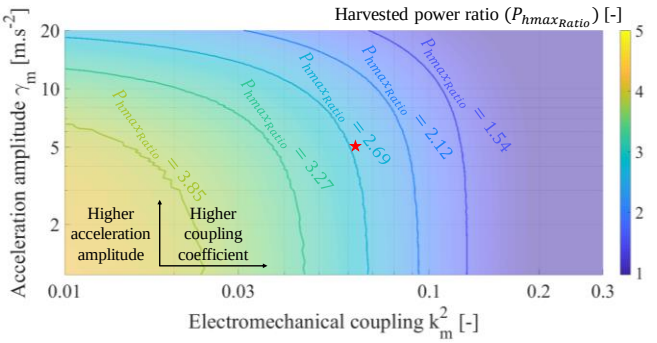

Figure 15 Maximum harvested power ratio ($P_{hmax_{Ratio}}$) as defined in (28), as a function of the acceleration amplitude and the electromechanical coupling. The red star corresponds to the acceleration amplitude and coupling conditions of the experimental tests. Warmer colors correspond to higher values of the harvested power ratio.

For this range of electromechanical coupling, the harvested power ratio also decreases as the acceleration amplitude increases going from 2.9 at $k_m^2 = 6\,\%$ and $\gamma_m = 1\,m.s^{-2}$ to 1.7 at $k_m^2 = 6\,\%$ and $\gamma_m = 20\,m.s^{-2}$. For strong electromechanical coupling ($6 - 30\,\%$), the harvested power ratio decreases as the electromechanical coupling increases. Note that, in this case, the acceleration amplitude has almost no impact on the harvested power ratio especially for very strong electromechanical coupling. Moreover, as shown in **Figure 15**, the maximum harvested power ratio is close to 2.4 for the three experimental acceleration amplitudes (red stars).

The figure of merit (FoM) presented in [29] is computed as the ratio of the power envelope integral over a given frequency range for the P-SSHI and the SEH circuits and can be expressed as:

$$FoM = \frac{\int_{f_{min}}^{f_{max}} P_{hmax_{PSSHI}} df}{\int_{f_{min}}^{f_{max}} P_{hmax_{SEH}} df} \qquad (29)$$

The FoM, as defined in (29), corresponds to the ratio of the area under the power envelope curve. This ratio reflects the performance gain of the P-SSHI circuit compared to the SEH: the higher the FoM, the higher the performance gain of the P-SSHI circuit. Note that the integration boundaries in (29), denoted as f_{min} and f_{max}, are respectively set to $5\,Hz$ and $200\,Hz$ for computing the values of the FoM. This choice is based on the observation that the harvested power at frequencies below $5\,Hz$ or above $200\,Hz$ is significantly low, and therefore does not impact the value of the integral. The FoM illustrated in **Figure 16** can be divided into 9 regions, depending on the electromechanical coupling and the acceleration amplitude. For weak electromechanical coupling ($1 - 3\,\%$) and weak acceleration amplitudes ($1 - 3\,m.s^{-2}$), the FoM value is greater than 5 which means the area under the power envelope curve of the P-SSHI circuit is 5 times larger than with the SEH circuit.

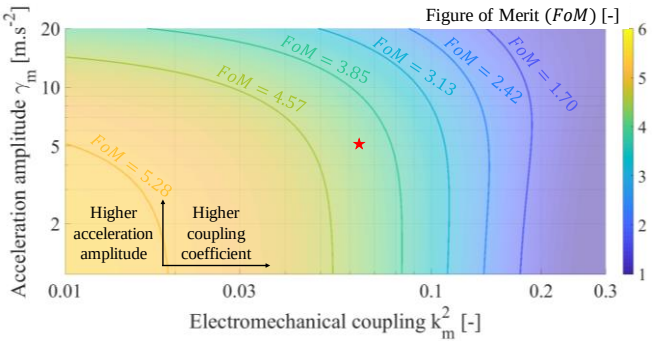

Figure 16 Figure of merit (FoM) as defined in (29), as a function of the acceleration amplitude and the electromechanical coupling. The red star corresponds to the acceleration amplitude and coupling conditions of the experimental tests. Warmer colors correspond to higher values of the figure of merit.

For medium acceleration amplitudes ($3 - 7\,m.s^{-2}$), the FoM value remains around 5. Further increase of the acceleration amplitude (up to $20\,m.s^{-2}$) tends to decrease the value of the FoM which is around 3.54 with $\gamma_m = 20\,m.s^{-2}$. Indeed, increasing the acceleration amplitude tends to increase the displacement amplitude of the mass which leads to a higher damping ratio β as shown from (15) and (22). Therefore, the harvested power ratio and the critical frequency both decrease, leading to a lower value of the FoM. Moreover, as presented in appendix B for the SEH circuit, the critical coupling increases as the acceleration amplitude increases. Since the damping ratio β is proportional to the electromechanical coupling k_m^2, the effect of the damping ratio is even more increased leading to lower FoM values under strong acceleration amplitudes. Considering medium electromechanical coupling ($3 - 6\,\%$), the FoM also tends to decrease whatever the value of the acceleration amplitude. Indeed, as for the acceleration amplitude, increasing the electromechanical coupling tends to increase the damping ratio β, as shown from (15) and (22), thus decreasing the FoM value. For this range of electromechanical coupling ($3 - 6\,\%$) and weak acceleration amplitudes ($1 - 3\,m.s^{-2}$), the value of the FoM remains close to 4.4 whereas it decreases up to 2.9 by increasing the acceleration amplitude up to $20\,m.s^{-2}$. For strong electromechanical coupling ($6 - 30\,\%$), the value of the FoM decreases as the electromechanical coupling increases. However, the acceleration amplitude has almost no impact on the FoM value especially for very strong electromechanical coupling. **Figure 16** shows that the P-SSHI allows to considerably enhance the performance of bistable PEH under weak electromechanical coupling and weak acceleration amplitudes. Moreover, as shown in **Figure 16**, the FoM value is within 4.3 ($\gamma_m = 5\,m.s^{-2}$) and 3.7 ($\gamma_m = 11\,m.s^{-2}$) for the experimental acceleration amplitudes (red stars). The performance of the proposed bistable PEH is therefore increased up to 4.3 using the P-SSHI circuit instead of the SEH circuit.

To summarize, the P-SSHI circuits brings a considerable performance gain compared to the SEH circuit, especially if the bistable PEH exhibits a weak electromechanical coupling ($1 - 5\,\%$) or the acceleration amplitude is quite low ($1 - 5\,m.s^{-2}$). For these range of acceleration amplitude and electromechanical coupling, the performance gain of the P-SSHI is higher than 5. It is essential to note that the theoretical optimal scenario for maximizing harvested power occurs when the PEH is strongly coupled. In such case, the SEH circuit will outperform the P-SSHI circuit. However, even with relatively strong coupling prototype such as the one used in this study ($k_m^2 = 6.3\,\%$), the P-SSHI circuit remains the preferred choice, with a FoM value higher than 3.

Table 2 Performance gain of the P-SSHI circuit compared to the SEH

Performance gain of the P-SSHI circuit			
	Weak coupling	Medium coupling	Strong coupling
Strong acceleration	+	=	=
Medium acceleration	++	+	=
Weak acceleration	+++	++	=

Moreover, due to various technical constraints, such as the use of lead-free piezoelectric material [32] or MEMS integration [33], the coupling may be further limited, making the P-SSHI circuit a valuable solution for enhancing harvested power and bandwidth. Considering the bandwidth gain, the P-SSHI circuit allows to widen the energy harvested bandwidth up to 2.3 compared to the SEH circuit. However, the electromechanical coupling range for which the bandwidth is highly increased ($B_{w_{Ratio}} > 2.07$) is different from the range for which the harvested power is highly increased ($P_{h_{maxRatio}} > 3.85$). Therefore, a trade-off must be found between increasing the bandwidth and increasing the harvested power. Moreover, increasing the acceleration amplitude slightly decreases the performance gain, however even under strong acceleration amplitudes, the P-SSHI remains more efficient than the SEH for bistable PEH. It is also shown that there is a critical electromechanical coupling above which the performance gain is no longer as interesting. The performance gain of the P-SSHI compared to the SEH, based on the FoM, is summarized in **Table 2**. Focusing on the orange cells of **Table 2**, and considering the efficiency of the P-SSHI circuit, it is better to use the SEH circuit. Moreover, it is possible to switch off the control signal of the P-SSHI circuit, which is an excellent way to combine the advantages of both circuits as a function of the frequency and the acceleration amplitude. Note that, contrarily to the SEH circuit, the P-SSHI needs to be self-powered. However, self-powered implementations of the P-SSHI circuit have already been proposed in the literature [34][35], featuring power consumption in the range of a few μW to a few tens of μW. With our prototype, the power consumption would account for less than 1 % of the harvested power.

5. Conclusion

Due to their complex dynamics, bistable piezoelectric energy harvesters remain mostly numerically studied. However, such studies may hinder the physical understanding of these complex systems. In this study, simple analytical expressions of the critical frequency, harvested power, electrically induced damping and damping ratio for both the P-SSHI and the SEH circuits have been proposed. The experimental validation is in good agreement with the proposed models. These models, valid for the inter-well motion of the bistable PEH allow to physically understand the influence of the P-SSHI and the SEH circuits on the dynamics of the bistable PEH. When dealing with bistable PEH, the P-SSHI circuit allows a significant increase of the harvested power at low vibration frequency and enhances the bandwidth of the harvester. However, for relatively high vibration frequency, (above $60\ Hz$ in this study), the benefit of the P-SSHI circuit in terms of power is limited. Moreover, the higher the electromechanical coupling, the narrower the frequency range in which the P-SSHI circuit increases the harvested power. These points are of particular interest since they fundamentally differ from conclusions drawn for linear PEH combined with the P-SSHI circuit [36]. Indeed, in the case of linear PEH, the P-SSHI circuit does not have much impact on the bandwidth [29]. Additionally, in the linear case, the power improvement brought by the P-SSHI circuit is not limited to a specific frequency range.

The comparison of the performance of the two EECs allows to identify the conditions (acceleration amplitude and electromechanical coupling) for which the P-SSHI circuit is more efficient than the SEH circuit. This comparison shows that the P-SSHI circuit allows to considerably increase the performance of the bistable PEH especially when the PEH exhibits a weak electromechanical coupling ($1-5$ %) or the acceleration amplitude is weak ($1-5\ m.s^{-2}$). The harvested power can be increased up to 4.3 times for weak electromechanical coupling (1 %) and low acceleration amplitude ($1\ m.s^{-2}$). The bandwidth is increased up to 2.3 times ($k_m^2 = 13$ % and $\gamma_m = 3.6\ m.s^{-2}$). The models show that the parameters maximizing the harvested power differ from those maximizing the bandwidth thus demonstrating a trade-off between bandwidth and harvested power.

With a physical understanding of the influence of each parameter, the proposed models might help in sizing bistable PEH for real applicative cases in order to maximize the harvested power and the energy harvesting bandwidth. In future works, it could be interesting to merge the performance of both the SSHI and the SEH circuit. Since the SEH exhibits a larger harvested power for vibration frequencies above $60\ Hz$ due to a higher efficiency than the P-SSHI circuit, it could be interesting to switch on or off the control signal of the transistors depending on the vibration frequency. Moreover, a hybrid SSHI circuit combining both the advantages of a series and a parallel SSHI could be interesting as a cold-start for a self-powered circuit. In addition to the proposed developments, a maximum power point tracking algorithm could be implemented in order to even increase the harvested power and the bandwidth of bistable piezoelectric energy harvester.

Acknowledgements

This work has been supported by the French government under the Future Investment Program (Programme d'Investissement d'Avenir).

Data availability statement

The data that support the findings of this study are available upon request from the authors.

References

[1] Q. Wen, X. He, Z. Lu, R. Streiter, and T. Otto, "A comprehensive review of miniatured wind energy harvesters," Nano Materials Science, vol. 3, no. 2, pp. 170–185, Jun. 2021, doi: 10.1016/j.nanoms.2021.04.001.

[2] D. Hao et al., "Solar energy harvesting technologies for PV self-powered applications: A comprehensive review," Renewable Energy, vol. 188, pp. 678–697, Apr. 2022, doi: 10.1016/j.renene.2022.02.066.

[3] M. F. Sanad, A. E. Shalan, S. O. Abdellatif, E. S. A. Serea, M. S. Adly, and Md. A. Ahsan, "Thermoelectric Energy Harvesters: A Review of Recent Developments in Materials and Devices for Different Potential Applications," Top Curr Chem (Z), vol. 378, no. 6, p. 48, Dec. 2020, doi: 10.1007/s41061-020-00310-w.

[4] X. Lu, P. Wang, D. Niyato, D. I. Kim, and Z. Han, "Wireless Networks with RF Energy Harvesting: A Contemporary Survey," IEEE Commun. Surv. Tutorials, vol. 17, no. 2, pp. 757–789, 2015, doi: 10.1109/COMST.2014.2368999.

[5] G. K. Ottman, H. F. Hofmann, A. C. Bhatt, and G. A. Lesieutre, "Adaptive piezoelectric energy harvesting circuit for wireless remote power supply," IEEE Trans. Power Electron., vol. 17, no. 5, pp. 669–676, Sep. 2002, doi: 10.1109/TPEL.2002.802194.

[6] D. Guyomar, A. Badel, E. Lefeuvre, and C. Richard, "Toward energy harvesting using active materials and conversion improvement by nonlinear processing," IEEE Trans. Ultrason., Ferroelect., Freq. Contr., vol. 52, no. 4, pp. 584–595, Apr. 2005, doi: 10.1109/TUFFC.2005.1428041.

[7] E. Lefeuvre, A. Badel, C. Richard, and D. Guyomar, "Piezoelectric Energy Harvesting Device Optimization by Synchronous Electric Charge Extraction," Journal of Intelligent Material Systems and Structures, vol. 16, no. 10, pp. 865–876, Oct. 2005, doi: 10.1177/1045389X05056859.

[8] M. Lallart, L. Garbuio, L. Petit, C. Richard, and D. Guyomar, "Double synchronized switch harvesting (DSSH): a new energy harvesting scheme for efficient energy extraction," IEEE Trans. Ultrason., Ferroelect., Freq. Contr., vol. 55, no. 10, pp. 2119–2130, Oct. 2008, doi: 10.1109/TUFFC.912.

[9] P. Gasnier et al., "An Autonomous Piezoelectric Energy Harvesting IC Based on a Synchronous Multi-Shot Technique," IEEE J. Solid-State Circuits, vol. 49, no. 7, pp. 1561–1570, Jul. 2014, doi: 10.1109/JSSC.2014.2325555.

[10] M. Lallart, W.-J. Wu, L. Yan, and S.-W. Hung, "Inductorless Synchronized Switch Harvesting Using a Piezoelectric Oscillator," IEEE Trans. Power Electron., vol. 35, no. 3, pp. 2585–2594, Mar. 2020, doi: 10.1109/TPEL.2019.2925709.

[11] S. C. Stanton, C. C. McGehee, and B. P. Mann, "Nonlinear dynamics for broadband energy harvesting: Investigation of a bistable piezoelectric inertial generator," Physica D: Nonlinear Phenomena, vol. 239, no. 10, pp. 640–653, May 2010, doi: 10.1016/j.physd.2010.01.019.

[12] A. Erturk and D. J. Inman, "Broadband piezoelectric power generation on high-energy orbits of the bistable Duffing oscillator with electromechanical coupling," Journal of Sound and Vibration, vol. 330, no. 10, pp. 2339–2353, May 2011, doi: 10.1016/j.jsv.2010.11.018.

[13] A. Morel et al., "Simple analytical models and analysis of bistable vibration energy harvesters," Smart Mater. Struct., vol. 31, no. 10, p. 105016, Oct. 2022, doi: 10.1088/1361-665X/ac8d3d.

[14] C. Lan, Y. Liao, G. Hu, and L. Tang, "Equivalent impedance and power analysis of monostable piezoelectric energy harvesters," Journal of Intelligent Material Systems and Structures, vol. 31, no. 14, pp. 1697–1715, Aug. 2020, doi: 10.1177/1045389X20930080.

[15] S. Bae and P. Kim, "Load Resistance Optimization of a Broadband Bistable Piezoelectric Energy Harvester for Primary Harmonic and Subharmonic Behaviors," Sustainability, vol. 13, no. 5, p. 2865, Mar. 2021, doi: 10.3390/su13052865.

[16] Q. Demouron, A. Morel, D. Gibus, A. Benhemou, and A. Badel, "Resistive Load Influence on the Power and Bandwidth of Bistable Energy Harvesters," in 2022 IEEE 7th Forum on Research and Technologies for Society and Industry Innovation (RTSI), Paris, France, Aug. 2022, pp. 198–203. doi: 10.1109/RTSI55261.2022.9905162.

[17] K. A. Singh, R. Kumar, and R. J. Weber, "A Broadband Bistable Piezoelectric Energy Harvester With Nonlinear High-Power Extraction," IEEE Trans. Power Electron., vol. 30, no. 12, pp. 6763–6774, Dec. 2015, doi: 10.1109/TPEL.2015.2394392.

[18] T. Huguet, M. Lallart, and A. Badel, "Bistable vibration energy harvester and SECE circuit: exploring their mutual influence," Nonlinear Dyn, vol. 97, no. 1, pp. 485–501, Jul. 2019, doi: 10.1007/s11071-019-04993-9.

[19] J. Wang, B. Zhao, W.-H. Liao, and J. Liang, "New insight into piezoelectric energy harvesting with mechanical and electrical nonlinearities," Smart Mater. Struct., vol. 29, no. 4, p. 04LT01, Apr. 2020, doi: 10.1088/1361-665X/ab7543.

[20] T. Huguet, A. Badel, and M. Lallart, "Parametric analysis for optimized piezoelectric bistable vibration energy harvesters," Smart Mater. Struct., vol. 28, no. 11, p. 115009, Nov. 2019, doi: 10.1088/1361-665X/ab45c6.

[21] V. G. Cleante, M. J. Brennan, G. Gatti, and D. J. Thompson, "On the target frequency for harvesting energy from track vibrations due to passing trains," Mechanical Systems and Signal Processing, vol. 114, pp. 212–223, Jan. 2019, doi: 10.1016/j.ymssp.2018.05.003.

[22] N. Cohen, I. Bucher, and M. Feldman, "Slow-fast response decomposition of a bi-stable energy harvester," Mechanical Systems and Signal Processing, vol. 31, pp. 29–39, Aug. 2012, doi: 10.1016/j.ymssp.2012.04.011.

[23] C. Saint-Martin, A. Morel, L. Charleux, E. Roux, A. Benhemou, and A. Badel, "Power expectation as a unified metric for the evaluation of vibration energy harvesters," Mechanical Systems and Signal Processing, vol. 181, p. 109482, Dec. 2022, doi: 10.1016/j.ymssp.2022.109482.

[24] T. Huguet, M. Lallart, and A. Badel, "Orbit jump in bistable energy harvesters through buckling level modification,"

Mechanical Systems and Signal Processing, vol. 128, pp. 202–215, Aug. 2019, doi: 10.1016/j.ymssp.2019.03.051.

[25] J. Wang, W.-H. Liao, and J. Cao, "Power enhancement of a monostable energy harvester by orbit jumps," Journal of Intelligent Material Systems and Structures, vol. 32, no. 20, pp. 2601–2614, Dec. 2021, doi: 10.1177/1045389X211006912.

[26] A. Morel, A. Badel, R. Grézaud, P. Gasnier, G. Despesse, and G. Pillonnet, "Resistive and reactive loads' influences on highly coupled piezoelectric generators for wideband vibrations energy harvesting," Journal of Intelligent Material Systems and Structures, vol. 30, no. 3, pp. 386–399, Feb. 2019, doi: 10.1177/1045389X18810802.

[27] Q. Demouron, A. Morel, D. Gibus, A. Benhemou, and A. Badel, "Resistive Load Influence on the Power and Bandwidth of Bistable Energy Harvesters," in 2022 IEEE 7th Forum on Research and Technologies for Society and Industry Innovation (RTSI), Paris, France, Aug. 2022, pp. 198–203. doi: 10.1109/RTSI55261.2022.9905162.

[28] R. L. Harne, M. Thota, et K. W. Wang, « Concise and high-fidelity predictive criteria for maximizing performance and robustness of bistable energy harvesters », Appl. Phys. Lett., vol. 102, nº 5, p. 053903, févr. 2013, doi: 10.1063/1.4790381.

[29] A. Morel et al., "A comparative study of electrical interfaces for tunable piezoelectric vibration energy harvesting," Smart Mater. Struct., vol. 31, no. 4, p. 045016, Apr. 2022, doi: 10.1088/1361-665X/ac54e8.

[30] Y. Liao and H. Sodano, "Optimal power, power limit and damping of vibration based piezoelectric power harvesters," Smart Mater. Struct., vol. 27, no. 7, p. 075057, Jul. 2018, doi: 10.1088/1361-665X/aabf4a.

[31] G. Clementi et al., "LiNbO3 films – A low-cost alternative lead-free piezoelectric material for vibrational energy harvesters," Mechanical Systems and Signal Processing, vol. 149, p. 107171, Feb. 2021, doi: 10.1016/j.ymssp.2020.107171.

[32] G. Clementi et al., "LiNbO3 films – A low-cost alternative lead-free piezoelectric material for vibrational energy harvesters," Mechanical Systems and Signal Processing, vol. 149, p. 107171, Feb. 2021, doi: 10.1016/j.ymssp.2020.107171.

[33] A. Sharma, O. Z. Olszewski, J. Torres, A. Mathewson, and R. Houlihan, "Fabrication, Simulation and Characterisation of MEMS Piezoelectric Vibration Energy Harvester for Low Frequency," Procedia Engineering, vol. 120, pp. 645–650, 2015, doi: 10.1016/j.proeng.2015.08.695.

[34] D. A. Sanchez, J. Leicht, F. Hagedorn, E. Jodka, E. Fazel, and Y. Manoli, "A Parallel-SSHI Rectifier for Piezoelectric Energy Harvesting of Periodic and Shock Excitations," IEEE J. Solid-State Circuits, vol. 51, no. 12, pp. 2867–2879, Dec. 2016, doi: 10.1109/JSSC.2016.2615008.

[35] S. Lu and F. Boussaid, "A Highly Efficient P-SSHI Rectifier for Piezoelectric Energy Harvesting," IEEE Trans. Power Electron., vol. 30, no. 10, pp. 5364–5369, Oct. 2015, doi: 10.1109/TPEL.2015.2422717.

[36] Y. C. Shu, I. C. Lien, and W. J. Wu, "An improved analysis of the SSHI interface in piezoelectric energy harvesting," Smart Mater. Struct., vol. 16, no. 6, pp. 2253–2264, Dec. 2007, doi: 10.1088/0964-1726/16/6/028.

Appendix A – Details of the experimental protocol set up in section 3

This appendix provides details on the experimental protocol applied to obtain the experimental data allowing to plot **Figure 8-14.** As presented in section 3, the experimental characterization of the bistable PEH is performed in the inter-well motion. The complete characterization of the bistable PEH is obtained for 30 resistances between $100\ \Omega$ and $10\ k\Omega$ and 90 frequencies between $25\ Hz$ and $67\ Hz$.

The experimental protocol for the bistable PEH characterization on the inter-well motion is illustrated in **Figure 17**. First, the excitation frequency is set to $50\ Hz$. Thereafter, depending on the setpoint the acceleration amplitude is gradually increased up to $9\ m.s^{-2}$. If the setpoint is lower than $9\ m.s^{-2}$, the acceleration amplitude is increased up to this value. The excitation frequency is then gradually decreased up to $25\ Hz$. During the decrease of the frequency, the prototype automatically jumps in the inter-well motion (the jump frequency strongly depends on the acceleration amplitude but remains within 25 and $50\ Hz$). The acceleration is finally gradually decreased back to the setpoint value so that the bistable PEH remains in the inter-well motion even though the acceleration amplitude is lower. In the case, the setpoint of the acceleration amplitude is equal or greater than $9\ m.s^{-2}$, the frequency is directly decreased up to $25\ Hz$ and the prototype automatically jumps on the inter-well motion. Thereafter, the forward frequency sweep is performed from $25\ Hz$ to $67\ Hz$ in order to characterize the inter-well motion of the bistable prototype. Note that the presented orbit jump sequence is performed each time a new resistance is characterized.

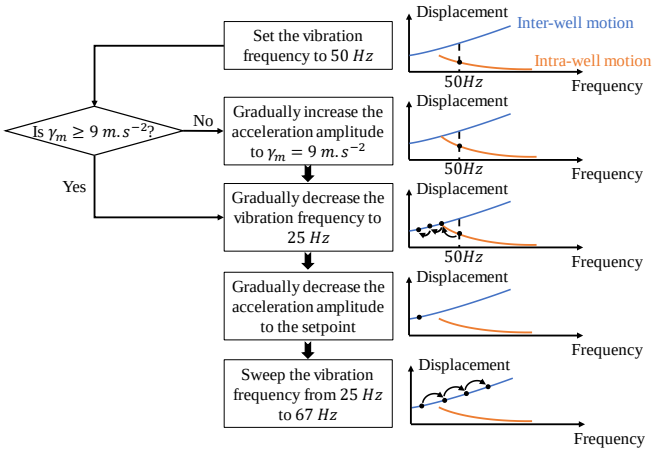

Figure 17 Experimental protocol for the bistable PEH characterization on the inter-well motion.

Appendix B – Critical electromechanical coupling and optimal resistance of the SEH circuit

This appendix provides details on the critical electromechanical coupling and the optimal resistance of the SEH and how they were obtained from the damping ratio β.

Solving $\beta_{SEH} = 1$, the following second order equation is obtained:

$$16\Omega^2 r^2 + \left(8\Omega\pi - \frac{8}{3}(1+2\Omega^2)k_m^2 Q\right) r + \pi^2 = 0 \quad (30)$$

Solving (30) leads to three different solutions depending on the electromechanical coupling:

$$\begin{cases} r_{opt} = \dfrac{\pi}{4\Omega} \forall k_m^2 \in [0; k_{m_c}^2[\\ r_{opt} = \dfrac{-3\Omega\pi + k_m^2 Q(1+2\Omega^2)}{12\Omega^2} \forall k_m^2 = k_{m_c}^2 \\ r_{opt} = \dfrac{(1+2\Omega^2)k_m^2 Q}{12\Omega^2}\left(1 \pm \sqrt{1 - \dfrac{6\Omega\pi}{(1+2\Omega^2)}} - \dfrac{3\Omega\pi}{(1+2\Omega^2)k_m^2 Q}\right) \\ \forall k_m^2 \in]k_{m_c}^2; +\infty] \end{cases} \quad (31)$$

From the third equation of (31) yields the expression of the critical electromechanical coupling:

$$k_{m_c}^2 = \frac{6\Omega\pi}{(1+2\Omega^2)Q} \quad (32)$$

From (32), it is shown that the critical electromechanical coupling depends on the frequency. Since the useful frequency range depends on the acceleration amplitude γ_m, the critical coupling also depends on the acceleration amplitude. Therefore, increasing the acceleration amplitude leads to an increase of the critical coupling.